JACS
JOURNAL OF THE AMERICAN CHEMICAL SOCIETY
Article
pubs.acs.org/JACS

Homologous Critical Behavior in the Molecular Frameworks $Zn(CN)_2$ and Cd(imidazolate)$_2$

Ines E. Collings,[†] Andrew B. Cairns,[†] Amber L. Thompson,[†] Julia E. Parker,[‡] Chiu C. Tang,[‡] Matthew G. Tucker,[§] Jadna Catafesta,[∥,⊥] Claire Levelut,[∥] Julien Haines,[⊥] Vladimir Dmitriev,[#] Philip Pattison,[#,▽] and Andrew L. Goodwin*[,†]

[†]Department of Chemistry, University of Oxford, Inorganic Chemistry Laboratory, South Parks Road, Oxford, OX1 3QR, United Kingdom

[‡]Diamond Light Source, Chilton, Oxfordshire, OX11 0DE, United Kingdom

[§]ISIS Facility, Harwell Science and Innovation Campus, Didcot, OX11 0QX, United Kingdom

[∥]Laboratoire Charles Coulomb, UMR−CNRS 5221, Université Montpellier 2, Place E. Bataillon, 34095, Montpellier Cedex 5, France

[⊥]Institut Charles Gerhardt, Équipe C2M, UMR−CNRS 5253, Université Montpellier 2, Place E. Bataillon, 34095, Montpellier Cedex 5, France

[#]Swiss-Norwegian Beamlines, ESRF, Polygone Scientifique Louis Néel, 6 rue Jules Horowitz, 38000, Grenoble, France

[▽]Crystallography Competence Centre, École Polytechnique Fédérale de Lausanne, BSP, CH-1015 Lausanne, Switzerland

Supporting Information

ABSTRACT: Using a combination of single-crystal and powder X-ray diffraction measurements, we study temperature- and pressure-driven structural distortions in zinc(II) cyanide ($Zn(CN)_2$) and cadmium(II) imidazolate ($Cd(im)_2$), two molecular frameworks with the anticuprite topology. Under a hydrostatic pressure of 1.52 GPa, $Zn(CN)_2$ undergoes a first-order displacive phase transition to an orthorhombic phase, with the corresponding atomic displacements characterized by correlated collective tilts of pairs of Zn-centered tetrahedra. This displacement pattern sheds light on the mechanism of negative thermal expansion in ambient-pressure $Zn(CN)_2$. We find that the fundamental mechanical response exhibited by $Zn(CN)_2$ is mirrored in the temperature-dependent behavior of $Cd(im)_2$. Our results suggest that the thermodynamics of molecular frameworks may be governed by considerations of packing efficiency while also depending on dynamic instabilities of the underlying framework topology.

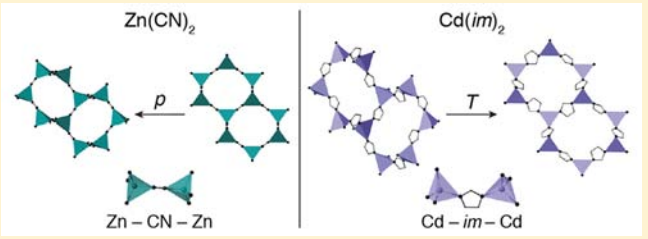

INTRODUCTION

From the soft-mode instabilities associated with ferroelectric transitions[1] to the crystalline−amorphous switching invoked in DVD-RAM technology,[2] critical phenomena lie at the very heart of practical applications of framework materials. It is an understanding of the physical driving forces behind phase transitions and the coupling of this critical behavior with electronic and magnetic degrees of freedom that has allowed enormous recent advances in the development of, e.g., multiferroic and magnetoresistive devices.[3] At its most straightforward, the study of critical phenomena involves identifying the existence and nature of temperature-, pressure-, or field-induced phase transitions, with the structural, electronic, and/or magnetic distortions involved invariably providing key insight into the physical properties of the material in question. Perhaps the archetypal example is that of cation off-centering in $BaTiO_3$:[4] the displacements associated with the high-temperature cubic−tetragonal phase transition in this material are precisely those responsible for its widely exploited ferroelectric, dielectric, and piezoelectric responses (currently a $2.5 billion industry in the U.S.A. alone).[5]

Historically, there has been a strong focus on understanding phase transition behavior in oxide-based ceramics, but there is an emerging realization that molecular frameworks, including many of the metal−organic frameworks (MOFs) usually studied for their gas sorption properties,[6,7] might display an equally rich variety of critical phenomena. Recent examples include multiferroicity, order−disorder transitions, and glassy behavior in transition-metal formates,[8−10] framework-breathing transitions in 'wine-rack'-like terephthalates and benzenedipyrazolates,[11,12] soft-mode displacive instabilities in functionalized lanthanide terephthalates,[13] and pressure- and temperature-induced amorphization in zeolitic imidazolate frameworks (ZIFs) and the canonical MOF-5.[14−17] The key advantage of molecular frameworks over "traditional" oxide-based ceramics is their enormous chemical versatility, which in principle allows

Received: February 4, 2013
Published: April 22, 2013

   dx.doi.org/10.1021/ja401268g | J. Am. Chem. Soc. 2013, 135, 7610−7620

for much greater control over functionality. Such an approach is exploited, e.g., in the use of chiral organic linkers to produce inherently acentric (and therefore piezoelectric) frameworks,[18] and the potential for host−guest interactions to couple functionality with sensing capabilities.[19]

But this same chemical versatility also means that the problem of determining "rules" governing critical behavior in molecular frameworks—precisely what is needed to direct intelligent materials development in this field—might almost appear intractable given that the choice of chemical components is essentially limitless. The situation is exacerbated further by the relative paucity of nonambient studies of molecular frameworks and also the inherent difficulties associated with computational studies for systems of such complex unit cell compositions.[20] The hope that such rules might even exist comes primarily from what is known of the behavior of traditional ceramics. In perovskite-like frameworks, for instance, there are a few key dynamical features that are essentially chemistry independent: the propensity for ferroelectric (zone-center) mode instabilities, together with the existence of zone-boundary soft modes that are ultimately responsible for the vast array of octahedral-tilting transitions permeating perovskite physics.[21] The chemistry of a given perovskite then dictates the interplay among these different features, but the fundamental mechanical response remains largely analogous throughout the one structural family.

So perhaps the fundamental question faced in the emerging field of molecular framework mechanics is the extent to which framework chemistry affects critical behavior for these systems. Or whether, like the perovskites, systems of the same network connectivity might exhibit similar mechanical responses. A number of earlier studies have shown that simple variations in, e.g., transition-metal character,[22−24] or ligand substitution patterns,[25] can give rise to well-understood variations in framework properties.

In this paper, we address the distinct problem of studying critical behavior in two isostructural molecular frameworks of very different chemistries. In particular we focus on the critical behavior of zinc(II) cyanide ($Zn(CN)_2$) and cadmium(II) imidazolate ($Cd(im)_2$): two molecular framework materials of particular currency in the field which share the same canonical anticuprite topology (Figure 1). Certainly there are differences in their quantitative behavior, but our key result is that the fundamental critical response is essentially the same for both systems. Specifically, pressure-induced transformations in the $Zn(CN)_2$ framework mirror the effect of lowering temperature on the structure of $Cd(im)_2$. Our results suggest that the thermodynamics of molecular frameworks are governed heavily by considerations of packing efficiency while also depending on dynamic instabilities of the underlying framework topology.

Zinc cyanide and cadmium imidazolate are important molecular frameworks in their own right, and so the implications of determining their critical behavior extend beyond the establishment of general sets of rules for molecular framework mechanics. On the one hand, $Zn(CN)_2$ is the parent compound in the most extreme family of negative thermal expansion (NTE) materials yet discovered.[26,27] Isotropic NTE (volume reduction on heating), such as that exhibited by $Zn(CN)_2$, remains incredibly rare and has important applications in the athermalization of high-precision optics.[28] The structural behavior of $Zn(CN)_2$ under pressure, which we characterize here, finally reveals the microscopic origin of its NTE response. On the other hand, $Cd(im)_2$ occupies a special

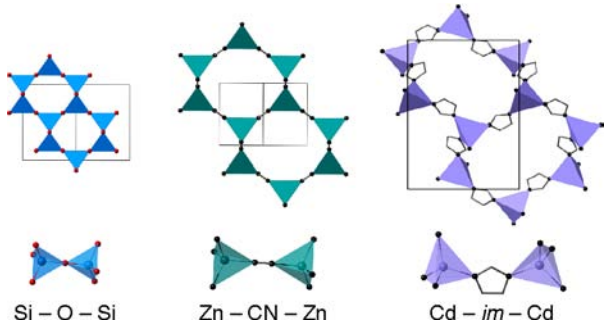

Figure 1. Crystal structures and coordination environments of frameworks with anticuprite-like topologies: (left−right) β-cristobalite, $Zn(CN)_2$, and $Cd(im)_2$. A constant scale is used for all diagrams. Both molecular frameworks are in fact doubly interpenetrated; one of the two networks has been omitted in this representation in order to accentuate the topological similarity among the three materials. Formally, the $Zn(CN)_2$ and $Cd(im)_2$ frameworks are topological equivalents of anticuprite (Cu_2O)—itself consisting of two interpenetrating cristobalite nets.

role in the ZIF family[29−31] as the lightest ZIF to adopt the canonical anticuprite topology.[32,33] We demonstrate that $Cd(im)_2$ also exhibits incredibly anomalous thermal expansion behavior, including extreme uniaxial-NTE that persists up to its decomposition temperature.

Our paper is arranged as follows. We begin by reporting the results of our high-pressure crystallographic study of $Zn(CN)_2$, including characterization of the structure and compressibility of its high-pressure phase $Zn(CN)_2$-II. The implications of the high-pressure behavior of $Zn(CN)_2$ for understanding NTE in this material are discussed. The high-pressure $Zn(CN)_2$ phase we identify is isostructural with the ambient phase of $Cd(im)_2$, and in the subsequent section we report our study of the variable-temperature behavior of this second molecular framework. What follows is an in-depth discussion of the parallels in critical behavior between the two systems. We draw comparisons in our analysis with the behavior of "traditional" oxide framework materials. Our manuscript concludes with a discussion of the implications of our study for the general understanding of mechanical behavior in molecular framework materials.

RESULTS

Zinc cyanide. Under ambient conditions $Zn(CN)_2$ adopts the anticuprite structure (space group $Pn\bar{3}m$), in which tetrahedral Zn^{2+} cations are connected via linear Zn−CN−Zn linkages to form a pair of interpenetrating diamondoid networks.[34−36] The cubic symmetry of this system means that its thermal expansion behavior is inherently isotropic. On heating, its cubic lattice parameter a (and hence volume V) decreases monotonically.[26,37] The magnitude of this NTE response can be quantified by the volume coefficient of thermal expansion:

$$\alpha_V = \frac{1}{V}\frac{dV}{dT} \quad (1)$$

taking the value $\alpha_V = -50.7(6)$ MK^{-1} over the temperature range 25−375 K.[26] By way of comparison, most materials expand on heating with coefficients of thermal expansion of around $\alpha_V = +30$ MK^{-1},[38] so this NTE effect is really very extreme and is much stronger than that observed for other well-

dx.doi.org/10.1021/ja401268g | J. Am. Chem. Soc. 2013, 135, 7610−7620

known NTE materials, such as ZrW_2O_8 ($\alpha_V = -27.3$ MK^{-1}; ref 39).

The thermodynamic anomaly responsible for driving NTE in systems such as $Zn(CN)_2$ is the existence of a large number of low-energy phonon modes with negative Grüneisen parameters $\gamma = -\mathrm{d} \ln \omega / \mathrm{d} \ln V$ (i.e., modes whose energies decrease with decreasing volume).[28] In the case of $Zn(CN)_2$, previous studies have often focused on correlated rotations of rigid $Zn(C/N)_4$ tetrahedra as the most likely NTE modes,[26,40−44] however analysis of polarization vectors obtained in density functional theory (DFT) phonon calculations indicates that some poorly understood translational component is also crucial.[45] In general, the expectation is that the NTE modes involve transverse displacements of the cyanide linkages away from the Zn···Zn axes, resulting in a reduction of the Zn···Zn separation and hence NTE. Because NTE modes decrease in energy with increasing pressure, it is very often the case that pressure-induced mode-softening leads to structural phase transitions in NTE materials.[46−49] Identification of the new modulations associated with such a transition then provides insight into the atomic displacements responsible for NTE in the parent phase.

No thermally induced structural transitions have been observed in $Zn(CN)_2$ either on cooling to 25 K or on heating to decomposition (~775 K).[26] In contrast, it is known that the ambient phase is only stable up to hydrostatic pressures of 0.6−1 GPa.[40,50] The compression behavior of ambient-phase $Zn(CN)_2$ is also anomalous: in particular, its bulk modulus $B = (-\mathrm{d} \ln V/\mathrm{d}p)^{-1}$ decreases with increasing pressure (i.e., the material becomes mechanically softer on compression), and moreover its coefficient of thermal expansion becomes increasingly negative at higher pressures.[50] This pair of observations is fully consistent with a picture in which the phonon modes responsible for NTE in the material are also those that soften most quickly on compression.

There is remarkably little consensus among previous studies concerning the nature of the high-pressure phases of $Zn(CN)_2$. The use of a hydrostatic pressure-transmitting medium (methanol/ethanol/water) produced a completely different series of phase transitions than was observed under non-hydrostatic conditions.[40] By virtue of the complex diffraction behavior observed, relatively little has been known other than that the observed transitions involve symmetry lowering (seen also in spectroscopic studies).[51] In preparation for this study, we found evidence for reaction of $Zn(CN)_2$ with the methanol/ethanol/water medium, a finding which almost certainly explains the discrepancies reported elsewhere.[40] Consequently for our own work we have used an H_2O-free methanol/ethanol mixture as pressure-transmitting medium, which we find not to react with $Zn(CN)_2$.

The pressure dependence we have measured for the unit cell parameters of $Zn(CN)_2$ is shown in Figure 2. Considering first the ambient phase $Zn(CN)_2$-I, a third-order Birch−Murnaghan (B-M) equation-of-state fit to our data gives values for the zero-pressure bulk modulus B_0 and its pressure derivative B' of 36.9(22) GPa and −8.6(13), respectively, that are in good agreement with those reported in ref 50 (namely, $B_0 = 34.19(21)$ GPa and $B' = -6.0(7)$). We find this ambient phase to persist up to 1.52 GPa, which extends well beyond the phase-transition pressures reported in previous studies using H_2O-containing mixtures as pressure-transmitting media. The negative value we obtain for B' reflects an anomalous decrease in bulk modulus with increasing pressure; moreover its magnitude is particularly extreme. By way of comparison,

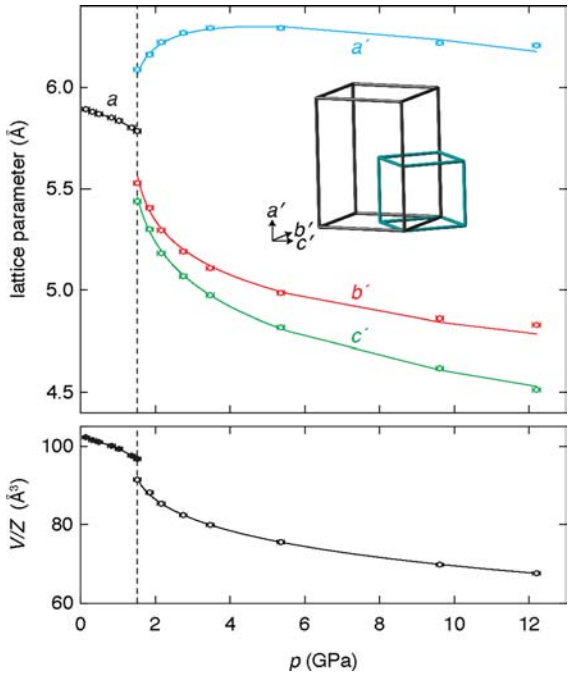

Figure 2. Evolution of the cubic (low pressure) and pseudocubic (high pressure) lattice parameters in $Zn(CN)_2$. The lines show fits to data using a third-order Birch−Murnaghan equation of state in the case of $Zn(CN)_2$-I and a modified version of the empirical expression given in ref 52 in the case of $Zn(CN)_2$-II (see SI). The pseudocubic lattice parameters of the high-pressure phase are related to the *Pbca* lattice parameters by $a' = a/2$, $b' = b/\sqrt{2}$, and $c' = c/\sqrt{2}$.

other systems that are known to exhibit such pressure-induced softening include $Zn[Au(CN)_2]_2$ and the mineral malayaite, for which $B' = -1.7(11)$ and −3(5), respectively.[53−55]

At a pressure of 1.52 GPa we observe the coexistence of the ambient $Pn\bar{3}m$ phase of $Zn(CN)_2$ with a new phase, which we term $Zn(CN)_2$-II. The diffraction profile of this high-pressure phase is shown in Figure 3; we note that the pattern is quite distinct to those reported previously for supposed high-pressure phases of $Zn(CN)_2$,[40] but is fully consistent with the orthorhombic polymorph reported in the parallel study of ref 41. We were able to index the diffraction pattern using an

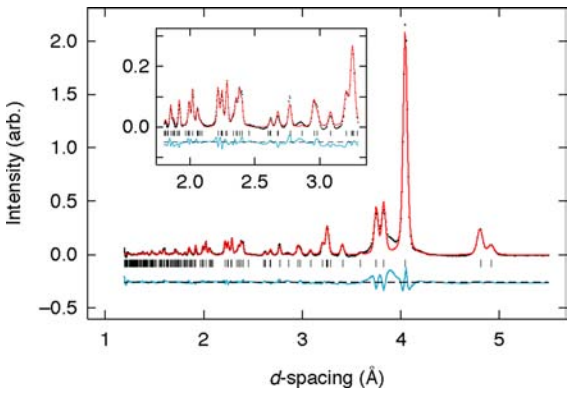

Figure 3. Synchrotron X-ray powder diffraction pattern (λ = 0.7092 Å) and Rietveld fit for data collected at a pressure of 1.85 GPa. Experimental data are given as points, the fitted profile as a solid red line, and the difference (data−fit) as a blue line, displaced downward vertically by 0.2 units. The inset shows a close-up of the fit obtained to the mid-*d* region of the diffraction pattern.

dx.doi.org/10.1021/ja401268g | J. Am. Chem. Soc. 2013, 135, 7610−7620

orthorhombic cell related to the cubic phase by the transformation:

$$\begin{bmatrix}\mathbf{a}\\ \mathbf{b}\\ \mathbf{c}\end{bmatrix}_{\text{ortho}} = \begin{bmatrix}0 & 0 & 2\\ 1 & 1 & 0\\ 1 & -1 & 0\end{bmatrix}\begin{bmatrix}\mathbf{a}\\ \mathbf{b}\\ \mathbf{c}\end{bmatrix}_{\text{cubic}} \quad (2)$$

The observed reflection conditions were consistent with assignment of the orthorhombic space group *Pbca*. Making use of the symmetry relationships between our $Pn\bar{3}m$ and *Pbca* cells we were able to arrive at a starting model for the structure of $Zn(CN)_2$-II, from which Rietveld refinement was possible for all our synchrotron X-ray data collected at pressures $1.52 < p < 12.2$ GPa (a representative fit is shown in Figure 3; fits to all collected data are provided as SI). The lattice parameters we obtain for this phase at 1.85 GPa (the first pressure point for which no scattering contribution from the ambient $Pn\bar{3}m$ phase was evident in our data) are $a = 12.3212(18)$ Å, $b = 7.6438(9)$ Å, $c = 7.4947(10)$ Å; corresponding atomic coordinates are listed in Table 1. For the data collected at the critical transition pressure $p_c = 1.52$ GPa itself, we were able to refine unit cell parameters for both phases: $V(Pn\bar{3}m)/Z = 193.515(22)$ Å^3 and $V(Pbca)/Z = 182.98(27)$ Å^3, suggesting a volume collapse of ~5% provides the necessary $p\Delta V$ free energy driving force responsible for the transition. The existence of such a volume discontinuity would suggest the transition is first order in nature.

Table 1. Atomic Coordinates and Isotropic Atomic Displacement Parameters in $Zn(CN)_2$-II Determined by Rietveld Refinement Against X-ray Powder Diffraction Data Collected at 1.85 GPa[a]

atom	x	y	z	U_{iso} (Å^2)
Zn1	0.1255(12)	0.0510(8)	0.7872(10)	0.069(4)
(C/N)1	−0.020(3)	0.118(4)	0.288(7)	0.079(9)
(C/N)2	0.0378(27)	0.236(4)	0.301(7)	0.079(9)
(C/N)3	0.2397(27)	0.018(7)	0.619(4)	0.079(9)
(C/N)4	0.286(4)	0.033(7)	0.487(4)	0.079(9)

[a]The atom labels "(C/N)" refer to sites with occupancy $C_{0.5}N_{0.5}$ and reflect the cyanide orientational disorder present in the compound.

Figure 4a illustrates the structural relationship between the phases $Zn(CN)_2$-I and $Zn(CN)_2$-II. The primary distortion associated with the I/II phase transition appears to involve concerted rotations of columns of $[Zn(C/N)_4]$ tetrahedra about axes parallel to the cubic ⟨110⟩ directions. The axis of rotation does not pass through the centers of individual tetrahedra, but rather through the midpoints of connected pairs of tetrahedra such that the Zn centers are translated in a direction perpendicular to the rotation axis. The implication here is that the key NTE modes of $Zn(CN)_2$-I involve translations of $Zn(C/N)_4$ tetrahedra in addition to the rotational modes already identified elsewhere;[26,44] an observation that is fully consistent with the DFT and neutron spectroscopy results that implicate the transverse acoustic modes in driving NTE.[22,44,45] Why this displacement pattern should give rise to NTE is also clear: Zn···Zn separations are reduced as the CN ions translate in a perpendicular direction to the Zn···Zn vectors (Figure 4b).

The group−subgroup relationship we observe here for the two phases $Zn(CN)_2$-I and $Zn(CN)_2$-II is not consistent with the softening of a single mode of the parent structure.[56]

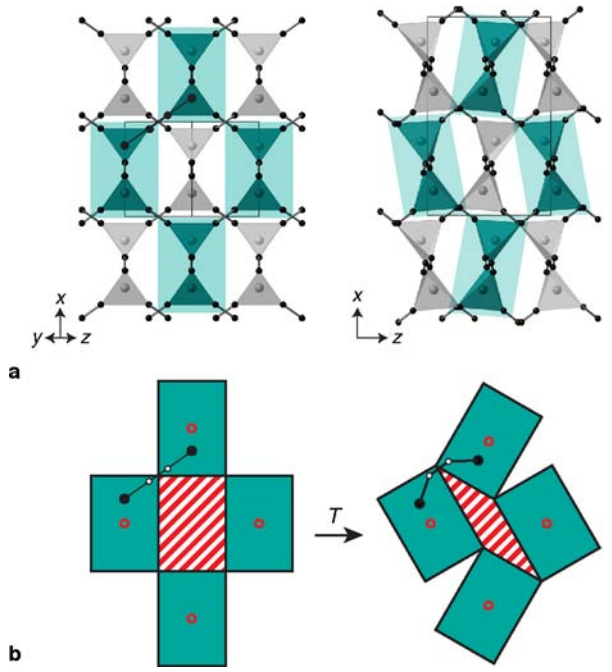

Figure 4. (a) The first-order phase transition between $Zn(CN)_2$-I (left) and $Zn(CN)_2$-II (right) involves concerted rotations of columns of $[Zn(C/N)_4]$ tetrahedra about axes that run parallel to ⟨110⟩ directions of the $Pn\bar{3}m$ cell and which pass the midpoints of neighboring tetrahedra. In this plan view, these displacements take the form of rotations of connected pairs of tetrahedra, as indicated by the shaded regions in the right-hand panel and as such involve translations of the Zn atoms along the horizontal axis. (b) The displacement pattern observed on pressure collapse also describes the key NTE modes of the ambient $Zn(CN)_2$ phase. The rotations shown in (a) give rise to transverse displacements of CN bridges away from the originally linear Zn−CN−Zn axes, resulting in a contraction of the Zn···Zn separation and a reduction in the extra-framework free volume (shaded region).

Consequently there is a possibility that the transformation occurs via an intermediate phase, although we have not found any experimental evidence for such a phase in our diffraction measurements. Indeed we even have access to a single data set (collected at a pressure of 1.52 GPa) where both phases I and II coexist and where there is no unaccounted for diffraction intensity (see SI). In light of the fact that the methanol/ethanol pressure-transmitting medium is still well within its hydrostatic regime at this pressure, this phase coexistence (which itself is likely a feature of relatively slow transformation kinetics) rules out the existence of a third, intermediate, phase.

The pressure dependence of the lattice parameters of $Zn(CN)_2$-II is shown in Figure 2. Unlike the ambient phase, this high-pressure phase stiffens at higher pressures. Despite this expected curvature of the $p(V)$ function, the data are not well represented by a second-order B-M equation-of-state ($B' \equiv 4$). Fitting to a third-order B-M equation-of-state fit is possible, but there is a very large correlation between B_0 and B' that prevents robust values from being determined. What we can say is that $Zn(CN)_2$-II is initially mechanically very soft on formation, but that the framework stiffens rapidly on further compression with $B' \gg 4$. Considering the linear compressibilities of the unit cell axes (and noting that these are coincident with the principal axes for an orthorhombic system), the most anomalous behavior is observed along **a**: on compression from $p_c = 1.52$ GPa the crystal actually expands

dx.doi.org/10.1021/ja401268g | J. Am. Chem. Soc. 2013, 135, 7610−7620

in this direction. This unusual negative linear compressibility (NLC) continues until a pressure of ~5 GPa, after which more usual positive linear compressibility (PLC) behavior is observed. This behavior is not without precedent in the broader family of molecular frameworks, where the interplay between geometric flexing and bond compression mechanisms is known to allow NLC–PLC transitions;[57] it is also reminiscent of the effects of structural reorganizations associated with second-order displacive transitions for the oxide-based frameworks GeO_2 and PbO_2.[58,59]

CADMIUM IMIDAZOLATE

Despite the different chemistries of the imidazolate and cyanide ions, the structure of $Cd(im)_2$ bears a close resemblance to that of $Zn(CN)_2$ and an even closer resemblance to the $Zn(CN)_2$-II high-pressure phase identified above. The structural relationship is straightforward: Cd centers replace Zn, and imidazolate anions occupy the CN^- sites.[32] In the ambient phase of $Cd(im)_2$, the Cd^{2+} coordination environment does not have ideal tetrahedral symmetry; nor are the Cd–*im*–Cd linkages linear. Consequently, the crystal structure is not that of the ideal $Pn\bar{3}m$ aristotype but instead has orthorhombic *Pbca* symmetry with the same supercell relationship as that given in eq 2. Just as $Zn(CN)_2$-II is a distorted variant of the parent $Zn(CN)_2$-I phase, so too might the ambient phase of $Cd(im)_2$ be considered a distorted variant of a hypothetical $Pn\bar{3}m$ parent.

The current interest in $Cd(im)_2$ comes primarily from its canonical standing among the transition-metal bis(imidazolates)—a family of compounds of particular topicality within the materials chemistry community.[29−31] Their structures are generally related to those of the aluminosilicates, and so as a family they are providing a useful conceptual bridge between long-established and well-understood oxide frameworks and the ever-expanding world of MOFs.[20] Some imidazolates have zeolite topologies (the ZIFs); many of these particular compounds exhibit exceptional sorption behavior and thermal stabilities, finding potential application in key areas such as CO_2 sequestration.[30,31,33,60] Others are MOF analogues of glassy SiO_2: the ability to switch between crystalline (porous) and amorphous (nonporous) forms makes these amorphous ZIFs interesting candidates for encapsulation of radioactive waste.[16,17,61,62] Yet others, like $Cd(im)_2$ itself, are analogues of dense SiO_2 phases; this class is primarily of fundamental interest in developing a coherent understanding of the mechanical behavior of MOFs.[20]

Because the ambient phase of $Cd(im)_2$ already adopts a distorted structure,[63] we sought to investigate its mechanical behavior by varying thermodynamic parameters in a way that acts to *increase* symmetry. This strategy corresponds either to application of negative pressures or to increasing temperature. Given the aporosity of $Cd(im)_2$, and hence the experimental difficulty of applying internal (i.e., negative) pressure, we focus here instead on the temperature-dependent structural variations in $Cd(im)_2$.

Using a combination of variable-temperature single-crystal and powder X-ray diffraction, we measured the lattice parameter variation shown in Figure 5. Throughout the temperature range 100–680 K we do not observe any phase transition behavior; although for temperatures above ~600 K we observe decomposition to a range of products including CdO. Hence our reduced confidence in the lattice parameters obtained for temperatures above 650 K, where decomposition of the $Cd(im)_2$ phase accelerates (see SI). There are two

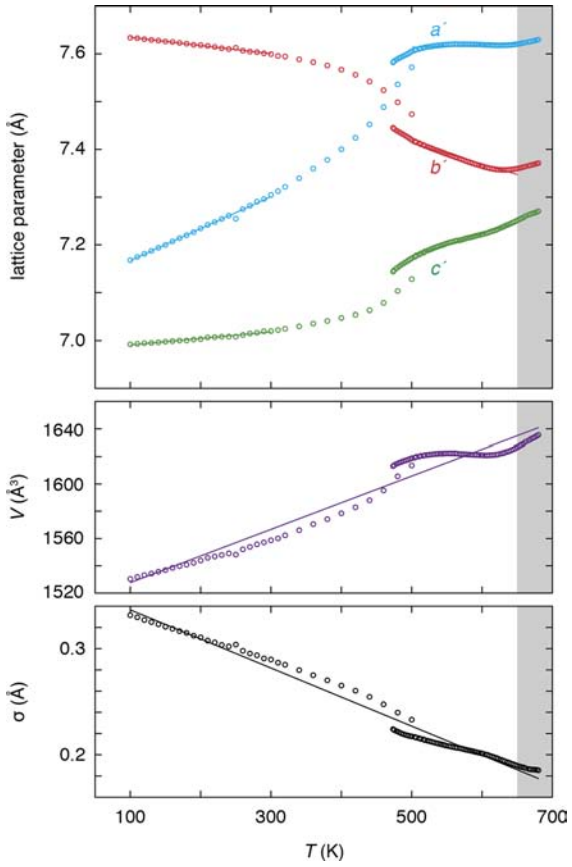

Figure 5. The upper panel illustrates the temperature-dependent pseudocubic lattice parameters for $Cd(im)_2$ as determined using a combination of single-crystal (100–500 K) and synchrotron powder (473–680 K) X-ray diffraction measurements. The slight discontinuities near 500 K reflect the different experimental conditions, and the shaded region above 650 K indicates those temperature values for which the diffraction data are affected by the contribution of decomposition products. The corresponding variation in unit cell volume is shown in the center panel, while the lower panel gives the corresponding thermal variation in standard deviation $\sigma(a',b',c')$ of the pseudocubic parameters. Despite the apparent nonlinearity of the thermal responses of individual lattice parameters, there is a continuous and linear tendency for increasing metric symmetry at higher temperatures. Extrapolation of the linear fit to these σ values suggests a *Pbca*–$Pn\bar{3}m$ transition temperature of ~1300 K.

immediate conclusions to be drawn from the data shown in Figure 5. First, the coefficients of thermal expansion are anomalous both in sign ($\alpha_b < 0$) and in magnitude ($|\alpha|$ values often greater than 50 MK^{-1}). Indeed the uniaxial NTE we observe here along the *b*-axis is notable even among the often extreme NTE coefficients observed in MOFs (Table 2). And, second, the uniaxial expansivity behaviors are highly nonlinear and anisotropic, despite an essentially linear overall (i.e., volume) expansivity. We proceed to explain the origin of these two effects.

A simple comparison of the structural models refined against our 100 and 650 K data reveals that the actual structural changes associated with increasing temperature are dominated by concerted rotations of columns of $[Cd(im)_4]$ tetrahedra about axes parallel to the [010] and [001] lattice vectors (both of which are equivalent to ⟨110⟩ directions in the hypothetical cubic parent) [Figure 6]. Indeed, the direct correspondence between this displacement pattern and that associated with the

dx.doi.org/10.1021/ja401268g | J. Am. Chem. Soc. 2013, 135, 7610–7620

Table 2. Linear Coefficients of Thermal Expansion in $Cd(im)_2$ and in Some NTE MOFs[a]

compound	axis	α (MK^{-1})	ref
$Cd(im)_2$	*a*	92.6(16); 6.5(11)	this work
	b	−22.5(5); −59.6(19)	
	c	19.6(7); 65.6(9)	
MOF-5	*a*	−16	64
HKUST-1	*a*	−7.5	65
Ag(*mim*)	~*a*	130(2)	57
	b	44(3)	
	~*c*	−24.5(8)	
HMOF-1	*a*	177(7)	66
	b	−21(3)	
	c	2.1(12)	
FMOF-1	*a*	230	67
	c	−170	

[a]The values given for $Cd(im)_2$ are determined over the two temperature ranges 100−300 and 500−650 K. Their (often large) differences reflect the strong nonlinearity apparent in the data as shown in Figure 5.

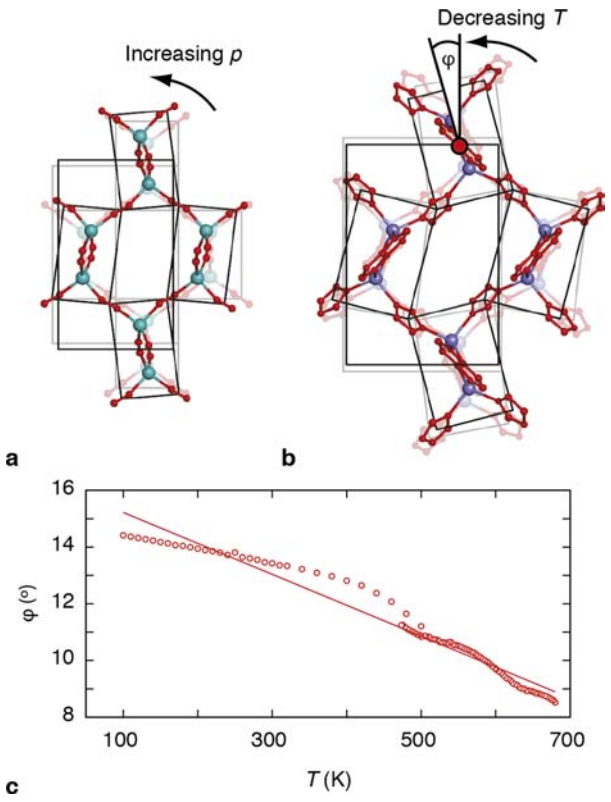

Figure 6. (a) The deformation mechanism associated with the pressure-induced $Zn(CN)_2$-I/II transition (and hence the displacement pattern responsible for driving NTE in $Zn(CN)_2$-I) is related to (b) the dominant temperature-dependent displacements observed in $Cd(im)_2$. The magnitude of these displacements can be quantified by the collective tilt angle φ (see SI). (c) The thermal variation in φ extracted from our structural refinements for $Cd(im)_2$ indicates a monotonic almost-linear reduction in tilt angle with increasing temperature. Extrapolation of a crude linear fit to these values (solid line) to $\varphi = 0$ gives an estimate of the hypothetical *Pbca*−$Pn\bar{3}m$ transition temperature of ~1500 K.

phase I/II transition in $Zn(CN)_2$ becomes the central focus of the Discussion section. But considering first the effect of these correlated rotations on the thermal expansion behavior, it is straightforward to show that the mean linear expansivity α_l to which they would correspond is given by the relationship

$$\alpha_l = -\tan\varphi \frac{d\varphi}{dT} \quad (3)$$

where φ is the mean rotation angle (Figure 6b). The derivation of this expression is given as SI. We find that the thermal variation of φ is approximately linear across the entire temperature range 100−650 K, reflecting a continual 'unfolding' of the network with increasing temperature (Figure 6c). Using eq 3 and the experimental values of $\langle\tan\varphi\rangle$ and $d\varphi/dT$, we obtain an effective $\alpha_l = +37.3(7)\ MK^{-1}$ that is remarkably similar to the experimental value $\alpha_l = \alpha_V/3 = +40.9(10)\ MK^{-1}$. Hence we can conclude that the bulk thermal response of $Cd(im)_2$ is driven by correlated (un)folding of the structure via a mechanism that is related to both the pressure-induced phase transition and the NTE effect in $Zn(CN)_2$. We note that extrapolation of the $\varphi(T)$ curve to $\varphi = 0$ (the point at which $Pn\bar{3}m$ symmetry would be recovered) suggests a transition temperature $T_c \simeq 1500$ K that lies well beyond the stability field of $Cd(im)_2$ at ambient pressure.

We now show that the anisotropy and nonlinearity observed in the thermal response of $Cd(im)_2$ are consequences of the reorganization of imidazolate orientations within the $[Cd(im)_4]$ coordination polyhedra. This is most clearly seen by considering the rectangular units obtained by projection of the 'rigid' $Cd(im)_2$ columns onto either the (010) or (001) planes, as illustrated in Figure 6. Idealized tetrahedral $[Cd(im)_4]$ geometries would give rectangular projections with an aspect ratio identically equal to $\sqrt{2}$; consequently, deviations from this ratio reflect geometric distortions of the tetrahedral units that arise either due to deformation of N−Cd−N bond angles or due to the inherent anisotropy of the imidazolate molecule. We find that at low temperatures these deviations are larger for the (001) plane (−6.0%) than for the (010) plane (+2.7%). So, on heating from 100 K the more severely distorted geometries are rectified first; this results in a contraction along **b** and a greater-than-anticipated expansion along **a** (Figure 7). The inflection points near 475 K seen in the lattice expansivity data of Figure 5 reflect the temperature at which the ideal ratio of $\sqrt{2}$ is achieved for the (001) system. It is unfortunate that this point also coincides approximately with the temperature extrema of our single-crystal and powder X-ray diffraction data; nevertheless there is good similarity in derived values for the small overlapping temperature range. At temperatures higher than this point the (010) system (which has become slightly more distorted during the first set of reorganizations) now becomes increasingly regular, resulting in an enhanced expansion along **c** and a much-reduced PTE effect along **a**. Hence the unusual lattice expansivities evident in Figure 5 reflect the activation of different reorganization mechanisms at different temperatures. If the degree of reorganization were very small, then each of the expansivities α_a, α_b, α_c, and $\alpha_l = \alpha_V/3$ would assume similar values. But even for large reorganizations the overall volume behavior is largely unaffected because a NTE effect along one axis is always balanced by a PTE effect along another axis. So the key point here is that at each stage the structure becomes increasingly symmetric at higher temperatures in a systematic manner, despite the nonlinearities in lattice parameter evolution.

As will be the case for many MOFs, the crystal structure of $Cd(im)_2$ is sufficiently complex that the full mechanical

dx.doi.org/10.1021/ja401268g | J. Am. Chem. Soc. 2013, 135, 7610−7620

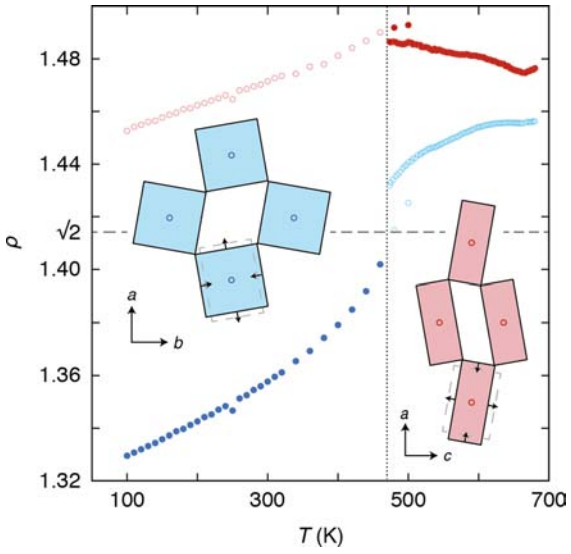

Figure 7. For ideally-tetrahedral metal coordination geometries the aspect ratio ρ of the rectangular units drawn in Figure 6 is equal to $\sqrt{2}$. Plotted here is the thermal variation of the corresponding ρ values for the (001) and (010) tilt systems in Cd(*im*)$_2$ (blue and red data points, respectively). At low temperatures, the (001) system is the more distorted, with $\rho \ll \sqrt{2}$; on heating this value is seen to increase, with the point of inflection corresponding to the point at which the value $\rho = \sqrt{2}$ is reached. There is no change in global symmetry at this point (hence ρ cannot "lock-on" to this value) because the (010) system remains distorted—in this case with $\rho > \sqrt{2}$. The second phase of reorganization ($T > 475$ K) is dominated by reduction of this second ρ value toward $\sqrt{2}$. The thermally activated increase in ρ for the (001) system results in an NTE effect along **b** and PTE along **a**; the corresponding decrease for the (010) system results in PTE along **c** and a NTE contribution along **a**.

response is a convoluted mix of variations in bond lengths and angles. Our analysis of a complete set of variable-temperature structural parameter data is provided as SI. As part of that same analysis we demonstrate the most important result—namely that the key aspects of the lattice parameter evolution are all explainable in terms of the correlated folding and molecular reorientation mechanisms described above.

We conclude our discussion of the lattice parameter variation in Cd(*im*)$_2$ by noting that the lattice parameters themselves also reflect a continuous transition toward increasing symmetry at higher temperatures. Figure 5 illustrates the temperature dependence of the measured standard deviation in pseudocubic lattice parameters $\sigma(a',b',c')$. The value of σ is equal to zero if and only if the *Pbca* lattice parameters correspond to those expected for the ideal cubic $Pn\bar{3}m$ parent structure. What is clear is that σ decreases monotonically with T despite the various competing trends amongst a',b',c' during the different temperature regimes. Extrapolation of the $\sigma(T)$ curve to $\sigma = 0$ gives an estimate of the temperature at which the hypothetical $Pn\bar{3}m$ structure would be reached. Here we obtain $T_c \simeq 1300$ K, which is remarkably consistent with the estimate derived above using the observed thermal variation in polyhedral tilts. Taken together, these results suggest there likely exists a common critical temperature at which both unit cell metric and Cd coordination geometries assume the symmetry of the $Pn\bar{3}m$ aristotype. The temperature estimates we derive here represent an upper bound to this critical point, by virtue of the discontinuity in order parameter evolution that would arise if the transition were first order in nature.

DISCUSSION

The crucial result of our study has been to demonstrate the correspondence in distortion mechanisms between Zn(CN)$_2$ and Cd(*im*)$_2$. By identifying the symmetry-breaking displacements that occur during the pressure-induced phase transition of Zn(CN)$_2$, we establish the dominant form of vibrational motion responsible for NTE in its ambient phase: namely a set of concerted tilts of columns of [Zn(C/N)$_4$] tetrahedra about the cubic ⟨110⟩ axes. This same displacement pattern dominates the thermal response of Cd(*im*)$_2$ and is therefore also a soft mode of its hypothetical $Pn\bar{3}m$ parent (which would consequently be expected to exhibit NTE). So in both cases—and irrespective of the different framework chemistry—the anticuprite aristotype exhibits a characteristic critical displacive instability.

But what fundamental chemical or physical driving force is responsible for activating this particular displacement pattern in both materials? Our starting point in answering this question is to consider the parallels between the structure of Zn(CN)$_2$-II and Cd(*im*)$_2$, and that of the brookite polymorph of TiO$_2$. Brookite also crystallizes in the *Pbca* space group; its structure can be considered as a hexagonal-close-packed (hcp) array of oxide ions with Ti^{4+} ions occupying half the octahedral holes (Figure 8a). While the coordination number of Ti^{4+} in brookite is six, and that of both Zn^{2+} in Zn(CN)$_2$-II and Cd^{2+} in Cd(*im*)$_2$ is four, there is nonetheless a direct correspondence among the anion/cation positions of each of the three structures. The distinction in coordination number comes

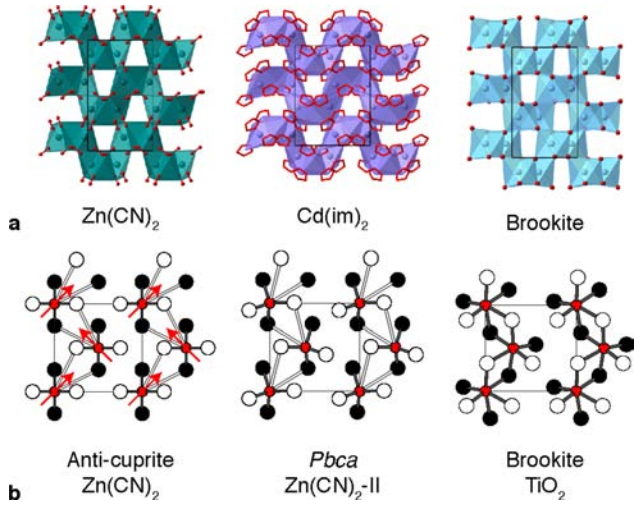

Figure 8. (a) The unit cell symmetry and positional coordinates of both Zn(CN)$_2$-II and Cd(*im*)$_2$ are related to those found in the brookite polymorph of TiO$_2$. The Zn/Cd coordination environments in the former compounds are extended to include two additional nearby ligands parallels the octahedral Ti^{4+} coordination in brookite. (b) The correspondence between anticuprite and brookite structures involves association of originally tetrahedral cations with two anions from a single neighboring tetrahedron to form connected chains that run perpendicular to the long **a** axis of the *Pbca* cell (the **a** axis is vertical in panel (a) while the schematics in (b) are drawn perpendicular to this same axis). Cations are shown as filled red circles and anions as open and filled black circles (positive and negative out-of-plane displacements, respectively, relative to cation positions). The square regions drawn here are guides to the eye but do have the same dimensions as the (100) face of the *Pbca* cell.

dx.doi.org/10.1021/ja401268g | J. Am. Chem. Soc. 2013, 135, 7610−7620

simply from molecular anion orientation and symmetry-allowed cation off-centering within the octahedral sites.

Importantly, the compression mechanism of $Zn(CN)_2$-II on increasing pressure and the collective reorganizations within $Cd(im)_2$ that occur on cooling both reflect a systematic transition away from the anticuprite geometry toward a brookite-like arrangement. That the anticuprite and brookite structures should be related by a relatively small and accessible set of atomic displacements is perhaps not immediately obvious. The general form of these displacements is illustrated in Figure 8b. Starting from the anticuprite structure, the cations move in a concerted manner toward a single edge of their tetrahedral coordination environment—the resulting position corresponds to the octahedral sites of the brookite structure. As an aside, we note that a similar mechanism (operating in reverse) has been observed for framework expansion in rutile-TiO_2 under negative pressure to give a tetrahedral TiO_2 net with the anticuprite topology.[68] By forming the vector dot product of the cation/anion displacements away from the ideal $Pn\bar{3}m$ sites with those observed in brookite itself, we can calculate an anticuprite/brookite order parameter Φ for $Zn(CN)_2$ and $Cd(im)_2$. The value of Φ is equal to zero for the ideal anticuprite geometry (i.e., no brookite-like displacements) and assumes increasingly large and positive values as the structures become more brookite-like. The evolution of Φ with increasing pressure ($Zn(CN)_2$-II) and decreasing temperature ($Cd(im)_2$) is illustrated in Figure 9a, where we have normalized the values such that max(Φ) = 1 for each data set. The similarity in critical behavior between the two systems is clear.

The drive toward brookite-like packing at high pressures and low temperatures can be viewed in two lights. On the one hand, there is the potential to increase the coordination number of the central cation as a means of improving packing efficiency and maximizing lattice enthalpy. An analysis of the pressure dependence of Zn−CN distances in $Zn(CN)_2$-II indicates a clear progression toward 6-fold coordination at high pressures that is associated with cation off-centering within the $[Zn(C/N)_4]$ tetrahedra (Figure 9b). A similar off-centering mechanism was recently identified in $Cd(CN)_2$, and we note here that the "ice rules" that govern Cd^{2+} displacements in that material are also obeyed in the anticuprite/brookite transition observed here for $Zn(CN)_2$ (see SI).[69] And, on the other hand, there is the simple consideration of packing efficiency of bulky anions. The anion arrangement in the $Pn\bar{3}m$ aristotype consists of square arrays; that in brookite is close packed (Figure 10). Whereas the focus within the MOF community is often (rightly) on the topological bonding connectivity of particular framework structures, what this observation highlights is that the physical packing arrangements might also play an important role in determining dynamical and mechanical response.

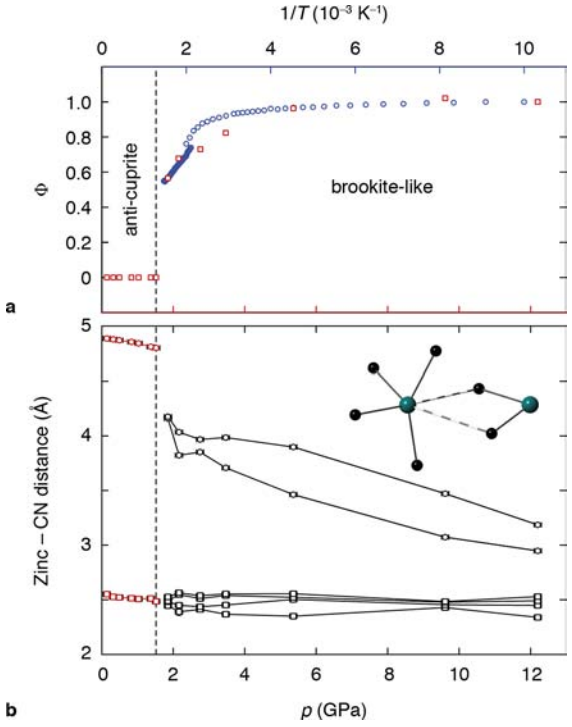

Figure 9. (a) Variation of the anticuprite/brookite order parameter Φ with increasing pressure ($Zn(CN)_2$; red squares) and decreasing temperature ($Cd(im)_2$; blue circles). (b) Pressure dependence of Zn−CN centroid separations in $Zn(CN)_2$. In the anticuprite $Zn(CN)_2$-I phase there are four well-defined nearest contacts which correspond to the $[Zn(C/N)_4]$ coordination polyhedra. Compression of the $Zn(CN)_2$-II phase does not involve significant changes in these four coordination distances. Rather, two further CN units approach increasingly closely, reflecting a systematic transition toward octahedral coordination, as suggested by the anticuprite−brookite mechanism illustrated in Figure 8b.

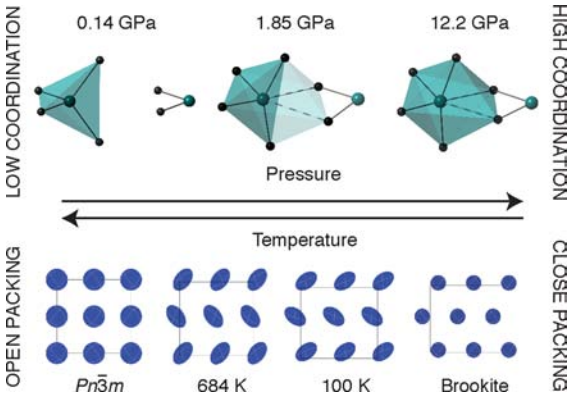

Figure 10. Critical behavior in $Zn(CN)_2$ and $Cd(im)_2$ can largely be understood by a tendency on the one hand to favor efficient packing at low temperatures or high pressures, and on the other hand to favor high-symmetry arrangements at low pressures or high temperatures.

■ CONCLUSIONS

The similarity in critical behavior between $Zn(CN)_2$ and $Cd(im)_2$ is important because it demonstrates the potential to establish a predictive and transferable understanding of dynamical response in molecular frameworks that is qualitatively independent of framework chemistry. It should be possible, for instance, to calculate generic phonon dispersion curves for aristotypic MOF topologies that highlight the existence and nature of soft modes that will likely play a dominant role in the mechanical response of all related networks. The role of framework chemistry then becomes one of tuning the energy scale and anharmonic sensitivity of these specific dynamic features. The nonlinear binding preference of the imidazolate anion, for instance, will lower the energy of transverse vibrational modes of the $Pn\bar{3}m$ $Cd(im)_2$ aristotype. Likewise, ligand substitution patterns will likely affect the periodicity with which certain low-energy displacements can most easily occur and hence favor softening at specific **k**-vectors.

dx.doi.org/10.1021/ja401268g | J. Am. Chem. Soc. 2013, 135, 7610−7620

In this sense there is much to be gained by extending the structural parallels currently drawn between MOF and oxide frameworks to a systematic comparison of dynamical response via the phonon dispersion relations. The anomalous mechanical behavior of ZIFs, for example, should be interpretable in terms of the dynamics of the corresponding zeolites. There will be complications, of course, such as the physical and electronic anisotropy of the molecular anions present in MOFs which result in molecular reorientation processes (as seen above for $Cd(im)_2$) that hinder direct interpretation of, e.g., lattice expansivities. But what we have demonstrated here is that the dominant mechanism of bulk response in molecular frameworks can be largely chemistry independent. So, just as our identification of the NTE mechanism in $Zn(CN)_2$ helps understand the thermal response of $Cd(im)_2$, one can now reasonably expect to establish meaningful correspondences among framework material function for systems of very different chemical composition.

METHODS

Sample Preparation. Single crystals of $Cd(im)_2$ were prepared via slow diffusion of aqueous solutions (~0.2 M) of cadmium(II) nitrate tetrahydrate (Sigma-Aldrich, 99%) and imidazole (Sigma-Aldrich, 99%). Deprotonation of the organic ligand was achieved by addition of a small quantity of ammonium hydroxide (Sigma-Aldrich, 99%). Crystals suitable for single-crystal X-ray diffraction experiments were obtained within 14 d. Polycrystalline samples of $Cd(im)_2$ were obtained by direct precipitation from stoichiometric mixing of aqueous solutions of cadmium(II) nitrate tetrahydrate and imidazole. The resulting precipitate was washed (H_2O), dried under vacuum, and finely ground.

The polycrystalline $Zn(CN)_2$ sample was purchased from Sigma-Aldrich (99%) and used as received.

Variable-Temperature Single-Crystal X-ray Diffraction. Variable-temperature single-crystal X-ray diffraction experiments were carried out on an Oxford Diffraction/Agilent SuperNova diffractometer (graphite-monochromated Mo Kα radiation, λ = 0.71073 Å) fitted with an Oxford Cryosystems Cryostream 600 open flow cooling device.[70] Data were collected on a single crystal (0.10 × 0.17 × 0.18 mm), mounted on a glass fiber with Araldite at room temperature, on cooling from 500 to 100 K at intervals of 20 K, and then on heating from 110 to 310 K at intervals of 20 K. For all data collections a single collection strategy was applied: namely, scanning through a full ω circle and collecting to a resolution of 0.77 Å.

Data indexing, reduction, and absorption corrections were performed using CrysAlisPro (Agilent). Initial structure solution was carried out with SIR92,[71] using the data collected at 100 K. Hydrogen atoms were added geometrically and regularized using standard restraints. Structure refinement (against $|F^2|$) was carried out using CRYSTALS.[72] Anisotropic thermal parameters were refined for all non-H atoms. This refined model was then used as a starting point for refinement against the 110 K data set. In this way, structure refinements for successive temperature points made use of the final model for the previous data set as a starting point. All refinements were carried out in an identical manner to that applied for the initial 100 K data set.

Variable-Temperature Powder X-ray Diffraction. Synchrotron X-ray powder diffraction data were collected at the high-resolution powder diffraction beamline I11 at the Diamond Light Source.[73] The sample was loaded in a 0.5 mm diameter borosilicate capillary and mounted in a horizontal spinner in the center of the beamline diffractometer. The sample temperature was controlled using a cyberstar hot air blower placed underneath the capillary. An initial data set was collected at a temperature of 200 °C, and the temperature was then ramped at a rate of 10 °C/min. The diffraction data were measured using a Mythen2 PSD (5 s exposures at two angular orientations offset by 0.25°),[74] resulting in a separation of approximately 3 °C between successive data sets. A polynomial background function, lattice constants, and atomic coordinates were refined using the Rietveld strategy as implemented within TOPAS (Academic Version 4.1).[75] The molecular geometry of imidazolate anions was fixed using rigid body constraints, and a soft Cd−N bond restraint (2.2 Å) was used to prevent unphysical imidazolate reorientations (X-rays being relatively insensitive to imidazolate orientations differing by 360°/5 by virtue of the weak C/N contrast).

Variable-Pressure Powder X-ray Diffraction. Synchrotron X-ray powder diffraction data were collected using the beamline BM01A of the Swiss-Norwegian Beamline, ESRF. All measurements were carried out at room temperature. An incident wavelength of 0.7092 Å was selected using a Si(111) monochromator, with focusing monochromator and mirror optics providing a focal spot of about 0.5 × 0.5 mm which was further reduced with slits to ~0.10 × 0.10 mm. The sample was loaded into a ETHZ standard diamond anvil cell, with a mixture of methanol/ethanol (4:1) as pressure-transmitting fluid and a ruby chip for pressure calibration. All data were collected with the mar345 image plate at a sample-to-detector distance of 250 mm. Initial frame exposure was for 60 s per frame (0−0.83 GPa), and the sample was stationary during the data collection. For data collected at pressures above 1 GPa the exposure time was increased to 180 s per frame. The distance and the detector parameters were calibrated using a LaB_6 reference powder sample, and calibration and subsequent integration were performed using fit2D.[76,77]

Rietveld refinement of these powder diffraction data was carried out using GSAS with $Zn(CN)_2$-I/-II models as appropriate.[78] The scale, background, peak shape parameters, lattice parameters, atomic positions, and isotropic displacement parameters (U_{iso}) were refined at each pressure on compression and decompression. Orientational disorder within the cyanide molecule was modeled by treating each C/N atom as a pair of carbon and nitrogen atoms with occupancy 0.5 and identical positional and displacement parameters. Soft C−N and Zn−(C/N) bond distance restraints were used for the refinement of $Zn(CN)_2$-II.

ASSOCIATED CONTENT

Supporting Information

Synthesis, crystallographic methods, single-crystal X-ray structural information, CIF files, variable pressure X-ray powder diffraction data and Rietveld fits, pressure-dependent lattice and structural parameter values. This information is available free of charge via the Internet at http://pubs.acs.org.

AUTHOR INFORMATION

Corresponding Author

andrew.goodwin@chem.ox.ac.uk

Notes

The authors declare no competing financial interest.

ACKNOWLEDGMENTS

The authors gratefully acknowledge financial support from the EPSRC (grant no. EP/G004528/2), the ERC (grant no. 279075), and the Agence Nationale de la Recherche (contract ANR-09-BLAN-0018-01). This work was carried out with the support of the Diamond Light Source and the European Synchrotron Radiation Facility.

REFERENCES

(1) Shirane, G.; Axe, J. D.; Harada, J.; Remeika, J. P. *Phys. Rev. B* **1970**, *2*, 155−159.
(2) Hegedüs, J.; Elliott, S. R. *Nat. Mater.* **2008**, *7*, 399−405.
(3) Cheong, S.-W.; Mostovoy, M. *Nat. Mater.* **2007**, *6*, 13−20.
(4) Zhang, Q.; Cagin, T.; Goddard, W. A., III *Proc. Natl. Acad. Sci., U.S.A.* **2006**, *103*, 14695−14700.

(5) Abraham, T.; McWilliams, A. Advanced Ceramics and Nanoceramic Powders. *BCC Research Report NAN015F*; BCC Research LLC: Wellesley, MA, 2011.
(6) Furukawa, H.; Ko, N.; Go, Y. B.; Aratani, N.; Choi, S. B.; Choi, E.; Yazaydin, A. Ö.; Snurr, R. Q.; O'Keeffe, M.; Kim, J.; Yaghi, O. M. *Science* **2010**, *329*, 424−428.
(7) Deng, H.; Grunder, S.; Cordova, K. E.; Valente, C.; Furukawa, H.; Hmadeh, M.; Gándara, F.; Whalley, A. C.; Liu, Z.; Asahina, S.; Kazumori, H.; O'Keeffe, M.; Terasaki, O.; Stoddart, J. F.; Yaghi, O. M. *Science* **2012**, *336*, 1018−1023.
(8) Jain, P.; Ramachandran, V.; Clark, R. J.; Zhou, H. D.; Toby, B. H.; Dalal, N. S.; Kroto, H. W.; Cheetham, A. K. *J. Am. Chem. Soc.* **2009**, *131*, 13625−13627.
(9) Xu, G.-C.; Ma, X.-M.; Zhang, L.; Wang, Z.-M.; Gao, S. *J. Am. Chem. Soc.* **2010**, *132*, 9588−9590.
(10) Besara, T.; Jain, P.; Dalal, N. S.; Kuhns, P. L.; Reyes, A. P.; Kroto, H. W.; Cheetham, A. K. *Proc. Natl. Acad. Sci., U.S.A.* **2011**, *108*, 6828−6832.
(11) Serre, C.; Bourrelly, S.; Vimont, A.; Ramsahye, N. A.; Maurin, G.; Llewellyn, P. L.; Daturi, M.; Filinchuk, Y.; Leynaud, O.; Barnes, P.; Férey, G. *Adv. Mater.* **2007**, *19*, 2246−2251.
(12) Salles, F.; Maurin, G.; Serre, C.; Llewellyn, P. L.; Knöfel, C.; Choi, H. J.; Filinchuk, Y.; Oliviero, L.; Vimont, A.; Long, J. R.; Férey, G. *J. Am. Chem. Soc.* **2010**, *132*, 13782−13788.
(13) Mowat, J. P. S.; Miller, S. R.; Griffin, J. M.; Seymour, V. R.; Ashbrook, S. E.; Thompson, S. P.; Fairen-Jimenez, D.; Banu, A.-M.; Düren, T.; Wright, P. A. *Inorg. Chem.* **2011**, *50*, 10844−10858.
(14) Hu, Y. H.; Zhang, L. *Phys. Rev. B* **2010**, *81*, 174103.
(15) Chapman, K. W.; Halder, G. J.; Chupas, P. J. *J. Am. Chem. Soc.* **2009**, *131*, 17546−17547.
(16) Bennett, T. D.; Goodwin, A. L.; Dove, M. T.; Keen, D. A.; Tucker, M. G.; Barney, E. R.; Soper, A. K.; Bithell, E. G.; Tan, J.-C.; Cheetham, A. K. *Phys. Rev. Lett.* **2010**, *104*, 115503.
(17) Bennett, T. D.; Keen, D. A.; Tan, J.-C.; Barney, E. R.; Goodwin, A. L.; Cheetham, A. K. *Angew. Chem., Int. Ed.* **2011**, *50*, 3067−3071.
(18) Yang, P.; He, X.; Li, M.-X.; Ye, Q.; Ge, J.-Z.; Wang, Z.-X.; Zhu, S.-R.; Shao, M.; Cai, H.-L. *J. Mater. Chem.* **2012**, *22*, 2398−2400.
(19) Halder, G. J.; Kepert, C. J.; Moubaraki, B.; Murray, K. S.; Cashion, J. D. *Science* **2002**, *298*, 1762−1765.
(20) Lewis, D. W.; Ruiz-Salvador, A. R.; Gómez, A.; Rodriguez-Albelo, M.; Coudert, F.-X.; Slater, B.; Cheetham, A. K.; Mellot-Draznieks, C. *CrystEngComm* **2009**, *11*, 2272−2276.
(21) Zhong, W.; Vanderblit, D. *Phys. Rev. Lett.* **1995**, *74*, 2587−2590.
(22) Chapman, K. W.; Hagen, M.; Kepert, C. J.; Manuel, P. *Physica B* **2006**, *385*−*386*, 60−62.
(23) Adak, S.; Daemen, L. L.; Hartl, M.; Williams, D.; Summerhill, J.; Nakotte, H. *J. Solid State Chem.* **2011**, *184*, 2854−2861.
(24) Galvelis, R.; Slater, B.; Cheetham, A. K.; Mellot-Draznieks, C. *CrystEngComm* **2012**, *14*, 374−378.
(25) Barburin, I. A.; Leoni, S. *J. Mater. Chem.* **2012**, *22*, 10152−10154.
(26) Goodwin, A. L.; Kepert, C. J. *Phys. Rev. B* **2005**, *71*, 140301.
(27) Phillips, A. E.; Goodwin, A. L.; Halder, G. J.; Southon, P. D.; Kepert, C. J. *Angew. Chem., Int. Ed.* **2008**, *47*, 1396−1399.
(28) Barerra, G. D.; Bruno, J. A. O.; Barron, T. H. K.; Allan, N. L. *J. Phys.: Condens. Matter* **2005**, *17*, R217−R252.
(29) Tian, Y.-Q.; Cai, C.-X.; Ren, X.-M.; Duan, C.-Y.; Xu, Y.; Gao, S.; You, X.-Z. *Chem. Eur. J.* **2003**, *9*, 5673−5685.
(30) Park, K. S.; Ni, Z.; Côté, A. P.; Choi, J. Y.; Huang, R.; Uribe-Romo, F. J.; Chae, H. K.; O'Keeffe, M.; Yaghi, O. M. *Proc. Natl. Acad. Sci., U.S.A.* **2006**, *103*, 10186−10191.
(31) Banerjee, R.; Phan, A.; Wang, B.; Knobler, C.; Furukawa, H.; O'Keeffe, M.; Yaghi, O. M. *Science* **2008**, *319*, 939−943.
(32) Tian, Y.-Q.; Xu, L.; Cai, C.-X.; Wei, J.-C.; Li, Y.-Z.; You, X.-Z. *Eur. J. Inorg. Chem.* **2004**, 1039−1044.
(33) Tian, Y.-Q.; Yao, S.-Y.; Gu, D.; Cui, K.-H.; Guo, D.-W.; Zhang, G.; Chen, Z.-X.; Zhao, D.-Y. *Chem. Eur. J.* **2010**, *16*, 1137−1141.
(34) Shugam, E.; Zhdanov, H. *Acta Physicochim. URSS* **1945**, *20*, 247−252.
(35) Hoskins, B. F.; Robson, R. *J. Am. Chem. Soc.* **1990**, *112*, 1546−1554.
(36) In this space group, the cyanide orientations are disordered throughout the structure such that the C and N atoms cannot be distinguished. The space group assignment has been verified independently by neutron scattering (ref 37) and spectroscopic measurements (refs 40 and 51).
(37) Williams, D.; Partin, D. E.; Lincoln, F. J.; Kouvetakis, J.; O'Keeffe, M. *J. Solid State Chem.* **1997**, *134*, 164−169.
(38) Okaji, M.; Yamada, N.; Moriyama, H. *Metrologia* **2000**, *37*, 165−171.
(39) Mary, T. A.; Evans, J. S. O.; Vogt, T.; Sleight, A. W. *Science* **1996**, *272*, 90−92.
(40) Poswal, H. K.; Tyagi, A. K.; Lausi, A.; Deb, S. K.; Sharma, S. M. *J. Solid State Chem.* **2009**, *182*, 136−140.
(41) Lapidus, S. H.; Halder, G. J.; Chupas, P. J.; Chapman, K. W. *J. Am. Chem. Soc.* **2013**, DOI: 10.1021/ja4012707.
(42) Chapman, K. W.; Chupas, P. J.; Kepert, C. J. *J. Am. Chem. Soc.* **2005**, *127*, 15630−15636.
(43) Goodwin, A. L. *Phys. Rev. B* **2006**, *74*, 134302.
(44) Zwanziger, J. W. *Phys. Rev. B* **2007**, *76*, 052102.
(45) Mittal, R.; Zbiri, M.; Schober, H.; Marelli, E.; Hibble, S. J.; Chippindale, A. M.; Chaplot, S. L. *Phys. Rev. B* **2011**, *83*, 024301.
(46) Evans, J. S. O.; Hu, Z.; Jorgensen, J. D.; Argyriou, D. N.; Short, S.; Sleight, A. W. *Science* **1997**, *275*, 61−65.
(47) Jorgensen, J. D.; Hu, Z.; Teslic, S.; Argyriou, D. N.; Short, S.; Evans, J. S. O.; Sleight, A. W. *Phys. Rev. B* **1999**, *59*, 215−225.
(48) Jorgensen, J. D.; Hu, Z.; Short, S.; Sleight, A. W.; Evans, J. S. O. *J. Appl. Phys.* **2001**, *89*, 3184−3188.
(49) Lind, C.; VanDerveer, D. G.; Wilkinson, A. P.; Chen, J.; Vaughan, M. T.; Weidner, D. J. *Chem. Mater.* **2001**, *13*, 487−490.
(50) Chapman, K. W.; Chupas, P. J. *J. Am. Chem. Soc.* **2007**, *129*, 10090−10091.
(51) Ravindran, T. R.; Arora, A. K.; Sairam, T. N. *J. Raman Spectrosc.* **2007**, *38*, 283−287.
(52) Goodwin, A. L.; Keen, D. A.; Tucker, M. G. *Proc. Natl. Acad. Sci., U.S.A.* **2008**, *105*, 18708−18713.
(53) Cairns, A. B.; Catafesta, J.; Levelut, C.; Rouquette, J.; van der Lee, A.; Peters, L.; Thompson, A. L.; Dmitriev, V.; Haines, J.; Goodwin, A. L. *Nat. Mater.* **2013**, *12*, 212−216.
(54) Rath, S.; Kunz, M.; Miletich, R. *Am. Mineral.* **2003**, *88*, 293−300.
(55) Cliffe, M. J.; Goodwin, A. L. *J. Appl. Crystallogr.* **2012**, *45*, 1321−1329.
(56) Hatch, D. M.; Stokes, H. T. In *XV International Colloquium on Group Theoretical Methods in Physics*; Gilmore, R., ed.; World Scientific: Singapore, 1987.
(57) Ogborn, J. M.; Collings, I. E.; Moggach, S. A.; Thompson, A. L.; Goodwin, A. L. *Chem. Sci.* **2012**, *3*, 3011−3017.
(58) Haines, J.; Léger, J. M.; Schulte, O. *J. Phys.: Condens. Matter* **1996**, *8*, 1631−1646.
(59) Haines, J.; Léger, J. M.; Chateau, C.; Pereira, A. S. *Phys. Chem. Miner.* **2000**, *27*, 575−582.
(60) Wang, B.; Côté, A. P.; Furukawa, H.; O'Keeffe, M.; Yaghi, O. M. *Nature* **2008**, *453*, 207−211.
(61) Chapman, K. W.; Sava, D. F.; Halder, G. J.; Chupas, P. J.; Nenoff, T. M. *J. Am. Chem. Soc.* **2011**, *133*, 18583−18585.
(62) Cao, S.; Bennett, T. D.; Keen, D. A.; Goodwin, A. L.; Cheetham, A. K. *Chem. Commun.* **2012**, *48*, 7805−7807.
(63) Masciocchi, N.; Ardizzoia, G. A.; Brenna, S.; Castelli, F.; Galli, S.; Maspero, A.; Sironi, A. *Chem. Commun.* **2003**, 2018−2019.
(64) Zhou, W.; Wu, H.; Yildirim, T.; Simpson, J. R.; Hight Walker, A. R. *Phys. Rev. B* **2008**, *78*, 054114.
(65) Wu, Y.; Kobayashi, A.; Halder, G. J.; Peterson, V. K.; Chapman, K. W.; Lock, N.; Southon, P. D.; Kepert, C. J. *Angew. Chem. Int. Ed.* **2008**, *47*, 8929−8932.
(66) DeVries, L. D.; Barron, P. M.; Hurley, E. P.; Hu, C.; Choe, W. *J. Am. Chem. Soc.* **2011**, *133*, 14848−14851.

(67) Yang, C.; Wang, X.; Omary, M. A. *Angew. Chem., Int. Ed.* **2009**, *48*, 2500−2505.
(68) Liu, Y.; Ni, L.; Ren, Z.; Xu, G.; Song, C.; Han, G. *J. Phys.: Condens. Matter* **2009**, *21*, 275901.
(69) Fairbank, V. E.; Thompson, A. L.; Cooper, R. I.; Goodwin, A. L. *Phys. Rev. B* **2012**, *86*, 104113.
(70) Cosier, J.; Glazer, A. M. *J. Appl. Crystallogr.* **1986**, *19*, 105−107.
(71) Altomare, A.; Cascarano, G.; Giacovazzo, C.; Guagliardi, A.; Burla, M.; Polidori, G.; Camalli, M. *J. Appl. Crystallogr.* **1994**, *27*, 435−436.
(72) Betteridge, P.; Carruthers, J.; Cooper, R. I.; Prout, K.; Watkin, D. J. *J. Appl. Crystallogr.* **2003**, *36*, 1487.
(73) Thompson, S. P.; Parker, J. E.; Potter, J.; Hill, T. P.; Birt, A.; Cobb, T. M.; Yuan, F.; Tang, C. C. *Rev. Sci. Instrum.* **2009**, *80*, 075107.
(74) Thompson, S. P.; Parker, J. E.; Marchal, J.; Potter, J.; Birt, A.; Yuan, F.; Fearn, R. D.; Lennie, A. R.; Street, S. R.; Tang, C. C. *J. Synchrotron Rad.* **2011**, *18*, 637−648.
(75) Coelho, A. A. *TOPAS (Academic Version 4.1)*; Coelho Software: Brisbane, Australia.
(76) Hammersley, A. P. *FIT2D: An Introduction and Overview*; ESRF: Grenoble, France, 1997.
(77) Hammersley, A. P.; Svensson, S. O.; Hanfland, M.; Fitch, A. N.; Häusermann, D. *High Press. Res.* **1996**, *14*, 235−248.
(78) Larson, A. C.; von Dreele, R. B. *General Structure Analysis System (GSAS)*; Los Alamos National Laboratory Report LAUR 86-748, 2004.